

Research Paper

Local Intratracheal Delivery of Perfluorocarbon Nanoparticles to Lung Cancer Demonstrated with Magnetic Resonance Multimodal Imaging

Lina Wu^{1*}, Xiaofei Wen^{1*}, Xiance Wang¹, Chunan Wang¹, Xilin Sun¹, Kai Wang¹, Huiying Zhang², Todd Williams², Allen J. Stacy², Junjie Chen², Anne H. Schmieder², Gregory M. Lanza², Baozhong Shen¹✉

1. Molecular Imaging Research Center (MIRC), Harbin Medical University, Harbin, Heilongjiang, China 2.TOF-PET/CT/MR center, The Fourth Hospital of Harbin Medical University, Harbin, Heilongjiang, China;
2. Department of Medicine, Division of Cardiology, Washington University School of Medicine, 4320 Forest Park Avenue, Saint Louis, MO 63108, USA.

* The authors contributed equally to this work.

✉ Corresponding author: Baozhong Shen MD, PhD, Professor of Department of Radiology of the Fourth Hospital of Harbin Medical University, Molecular Imaging Center of Harbin Medical University, 37 Yiyuan Street, Nangang District, Harbin, Heilongjiang 150001, China Phone: (86)-451-82576508; Fax: (86)-451-82576509 shenbzh@vip.sina.com

© Ivyspring International Publisher. This is an open access article distributed under the terms of the Creative Commons Attribution (CC BY-NC) license (<https://creativecommons.org/licenses/by-nc/4.0/>). See <http://ivyspring.com/terms> for full terms and conditions.

Received: 2017.06.14; Accepted: 2017.10.05; Published: 2018.01.01

Abstract

Eighty percent of lung cancers originate as subtle premalignant changes in the airway mucosal epithelial layer of bronchi and alveoli, which evolve and penetrate deeper into the parenchyma. Liquid-ventilation, with perfluorocarbons (PFC) was first demonstrated in rodents in 1966 then subsequently applied as lipid-encapsulated PFC emulsions to improve pulmonary function in neonatal infants suffering with respiratory distress syndrome in 1996. Subsequently, PFC nanoparticles (NP) were extensively studied as intravenous (IV) vascular-constrained nanotechnologies for diagnostic imaging and targeted drug delivery applications.

Methods: This proof-of-concept study compared intratumoral localization of fluorescent paramagnetic (M) PFC NP in the Vx2 rabbit model using proton (¹H) and fluorine (¹⁹F) magnetic resonance (MR) imaging (3T) following intratracheal (IT) or IV administration. MRI results were corroborated by fluorescence microscopy.

Results: Dynamic ¹H-MR and ¹⁹F-MR images (3T) obtained over 72 h demonstrated marked and progressive accumulation of M-PFC NP within primary lung Vx2 tumors during the first 12 h post IT administration. Marked ¹H and ¹⁹F MR signal persisted for over 72 h. In contradistinction, IV M-PFC NP produced a modest transient signal during the initial 2 h post-injection that was consistent circumferential blood pool tumor enhancement. Fluorescence microscopy of excised tumors corroborated the MR results and revealed enormous intratumor NP deposition on day 3 after IT but not IV treatment. Rhodamine-phospholipid incorporated into the PFC nanoparticle surfactant was distributed widely within the tumor on day 3, which is consistent with a hemifusion-based contact drug delivery mechanism previously reported. Fluorescence microscopy also revealed similar high concentrations of M-PFC NP given IT for metastatic Vx2 lung tumors. Biodistribution studies in mice revealed that M-PFC NP given IV distributed into the reticuloendothelial organs, whereas, the same dosage given IT was basically not detected beyond the lung itself. PFC NP given IT did not impact rabbit behavior or impair respiratory function. PFC NP effects on cells in culture were negligible and when given IV or IT no changes in rabbit hematology nor serum clinical chemistry parameters were measured.

Conclusion: IT delivery of PFC NP offered unique opportunity to locally deliver PFC NP in high concentrations into lung cancers with minimal extratumor systemic exposure.

Key words: perfluorocarbon nanoparticle, MRI, drug delivery, lung cancer, intratracheal delivery.

Introduction

Lung cancer is a leading cancer killer in both men and women in the US, in recent years surpassing breast cancer to become the leading cause of cancer death in women. Worldwide, lung cancer is the most common malignancy with ~1.8 million new cases and 1.6 million deaths annually [1]. Unfortunately, the five-year survival rate for lung cancer (17.8%) is notably less than for malignancies in the colon (65.4%), breast (90.5%) and prostate (99.6%) [2]. While patients diagnosed with early stage lung cancer have ~50% 5-year survival rate, the majority of individuals are diagnosed late and are dead within a year. This poor prognosis reflects the late presentation of clinical disease symptoms, including cough, hemoptysis, dyspnea, chest pain, or non-resolving pneumonia, that prompt patients to seek medical attention. Most lung cancer patients are diagnosed with non-small cell lung cancer (NSCLC) (87%) with the remaining malignancies attributed to small cell lung cancer [3].

80% of lung cancers originate as premalignant changes in the airway mucosal epithelial layer of bronchi and alveoli that progressively infiltrate into the underlying parenchyma [4]. Clinically silent, these small early lesions are typically beyond the resolution of computed tomography (CT), magnetic resonance (MR) or positron emission tomography/CT (PET/CT) to detect effectively. ^{18}F -fluorodeoxyglucose PET screening for lung cancer has a central role in disease staging and therapeutic response assessment, but the technique's diagnostic sensitivity is only 83% [5, 6]. Optical imaging via bronchoscopy is effective for evaluating premalignant epithelial mucosal lesions in the central airways, but the invasive technique can only interrogate six to seven generations of bronchi with the thinnest bronchoscopes [7], leaving the outer two-thirds of the lung inaccessible [8].

Traditional ^1H MRI is plagued by respiratory motion, air-tissue chemical-shift artifacts, and a low prevalence of tissue water protons when imaging the lung. However, promising advancements in MR pulmonary imaging using simultaneous proton and fluorine ($^1\text{H}/^{19}\text{F}$) MRI with ultrashort echo time sequences (UTE) have been implemented for preclinical models using clinical 3T MR scanners [9]. These emergent techniques optimized ^{19}F imaging and quantification by simultaneously acquiring proton and fluorine image data, allowing the more robust proton information to be used to optimize coil and power parameters and to correct for motion artifacts [9-11]. These technology advances have brought the opportunity for high-resolution, non-invasive, nonionizing MR imaging of the lung closer to the clinic.

Perfluorocarbon (PFC) nanoparticles (NP) are ~98% PFC with a high fluorine concentration of ~100 M [12]. Early preclinical and later clinical research with PFCs involved liquid breathing, taking advantage of the high oxygen-dissolving capacity of PFCs to overcome respiratory distress in preterm babies due to natural surfactant deficiencies [13-15]. Although PFC NP emulsions were clinically effective in neonates for this application, alternative surfactant replacement technologies soon emerged and supplanted their use [16, 17]. Cognizant of the oxygen-dissolving capacity and high biocompatibility of PFC emulsions, other investigators continued the clinical development of PFC NP as artificial blood substitutes [18]. During this timeframe, PFC NP research expanded to include GI bowel and general blood pool contrast uses for CT, MRI, and Doppler ultrasound [19-23].

The present research considers for the first time the use of PFC NP administered IT for diagnostic MR imaging of lung cancer in the Vx2 rabbit model. Given the high biocompatibility and liquid ventilation history of perfluorocarbon emulsions, the overarching hypothesis considered was whether prolonged IT exposure of lung cancers to PFC NP would afford deep locally-confined tumor penetration and strong $^1\text{H}/^{19}\text{F}$ MR signal. The objectives of this study were to: 1) demonstrate that PFC NP can be safely administered *via* IT delivery into rabbits with Vx2 lung cancer, 2) measure tumor temporal spatial differences in ^1H T1 mapping and ^{19}F MR imaging following IT vs. IV delivery of PFC NP with a clinically relevant scanner, 3) microscopically characterize PFC NP retention and distribution in tumor versus normal lung tissue regions, and 4) compare the biodistribution and bioelimination pathways of PFC NP given IT versus IV.

Materials and Methods

Chemicals

Unless otherwise listed, all solvents and reagents were purchased from Aldrich Chemical Co. and used as received. Phospholipids were purchased from Avanti Polar Lipids, Inc. (Alabama, USA). Argon gas (Ultra High Purity: UHP, 99.99%) was used to reduce oxidation of lipid materials and nanoparticle emulsions. Dialysis was performed with Spectra/Por membranes (Cellulose MWCO: 20,000 D, Spectrum Medical Industries, Inc.) Perfluoro-15-crown-5 ether (PFCE, $\text{C}_{10}\text{F}_{20}\text{O}_5$) was purchased from Exflur Research Corporation (Round Rock, TX) and used as acquired.

Preparation of multifunctional perfluorocarbon nanoparticles

Multifunctional paramagnetic PFC NP (M-PFC NP) incorporating a fluorescent lipid-anchored dye were synthesized using microfluidization similar to prior reports [24-26]. Briefly, the nanoparticulate emulsions were comprised of 20% (v/v) PFCE, 2% (w/v) of a surfactant commixture, 1.7% (w/v) glycerin and water representing the balance. The surfactant included 80 mol% dipalmitoyl phosphatidylcholine (DPPC), 10 mol% cholesterol, 5 mol% Gd-DTPA-phosphatidylethanolamine (Gd-DTPA-DPPE), 0.1 mol% 1,2-dipalmitoyl-sn-glycero-3-phosphoethanolamine-N-(lissaminerhodamine B sulfonyl) (ammonium salt) (16:0 LissRhod PE), and 4.9 mol% 1,2-dipalmitoyl-sn-glycero-3-phospho-(1'-rac-glycerol) (sodium salt). The lipids were dissolved in a mixture of methanol and chloroform, filtered through a small bed of cotton, evaporated under reduced pressure using a rotary evaporator at 45 °C to form a thin film, and then further dried in a vacuum oven (45 °C) for 24 h. The resuspended surfactant was combined with PFCE and water, then emulsified in a M110P Microfluidics emulsifier (Microfluidics, Newton, MA) at 20,000 psi for 4 min. The products were dialyzed against deionized water using a 20 kDa MWCO cellulosic membrane. The completed emulsions were placed in crimp-sealed vials, blanketed with argon, and stored at 4 °C until use.

Physical and chemical characterization of nanoparticles

Hydrodynamic diameter distribution, polydispersity, and zeta potential (ζ) of the PFC nanoparticles were determined by dynamic light scattering (DLS) with a Malvern Nano ZS Zetasizer (Malvern Instruments Ltd, Malvern, UK). All determinations were made in multiples of five consecutive measurements. Measurements of ζ were reproducible to within ± 4 mV of the mean value given by 16 determinations of 10 data accumulations. Atomic force microscopy measurements (AFM, Bruker Dimension Icon) were executed in standard tapping mode. UV/Vis absorption spectra were performed on a calibrated spectrophotometer (Perkin-Elmer Lambda 35) at room temperature.

The dissolved oxygen (O_2) and the release rate of O_2 in pure water and perfluorocarbon (20% v/v) solution were measured with a digital multi parameter meter (Multi 3430 WTW, Germany) coupled to an O_2 sensor (CellOx 325, WTW, Germany). Pre-test, the samples were ventilated with slowly bubbling O_2 for a predetermined duration. The measurements of the release rate of oxygen were performed with O_2 ventilation for 5 min, then airflow

was arrested and O_2 content was analyzed at baseline and every 5 min for 60 min thereafter.

Cellular toxicity of perfluorocarbon nanoparticles on bronchial epithelium

The cell viability of normal human bronchial epithelium BEAS-2B cells (ATCC[®] CRL-9609[™], Manassas, VA) and lung cancer H520 cells (ATCC[®] HTB-182[™]) were evaluated according to the manufacturer's instruction using the In-Situ Cell Death Detection Kit (Roche, Branchburg, NJ, USA). Cells were seeded in six-well cell culture plates in 2 mL medium with serum under 5% CO_2 at 37°C. Cells were washed with PBS three times then exposed in the recommended media to 9 mM or 90 mM M-PFC NP. After 24 h incubation, cells were washed three times with PBS and then evaluated for apoptosis with TUNEL diagnostic kit (EMD Millipore, Billerica, MA). The nuclei were stained with 4',6'-diamidine-2'-phenylindole dihydrochloride (DAPI, Sigma Aldrich, St. Louis, MO). Cells were imaged microscopically with an Olympus inverted fluorescence microscope (Olympus (Beijing) Sales & Service Co., Ltd., Beijing, China).

Flow cytometry assay

Normal epithelium cell BEAS-2B were grown in the presence of 9 mM M-PFC NPs for 24 h. Trypsinized cells were harvested and washed in cold PBS(3 \times), then isolated by centrifugation (1273 g for 5 min). Single cell suspensions were added to pre-chilled 75% ethanol and fixed at -20°C overnight. The cells were rinsed with phosphate buffer, resuspended, then post-fixed with Cell Cycle Assay KIT (Biyuntian Company, Shanghai, China). Flow cytometry was performed using a FACScan (Becton Dickinson, San Jose, CA) equipped with 488 nm and 633 nm lasers. Samples were gated to exclude debris and clumps, and electronic compensation was used to remove residual spectral overlap. The experiment was repeated in triplicate and data were analyzed using MultiCycle software WinCycle 32 (Phoenix Flow Systems, Inc., San Diego, CA).

Clinical pathology

Animal protocols were performed in accordance with the Guide for the Care and Use of Laboratory Animals published by the US National Institutes of Health (NIH publication No. 85-23, revised 1996) and were approved and monitored by the Harbin Medical University and Washington University Animal Care and Use Committee, respectively.

Clinical pathology was performed on two sets of KunMing white mice (20-25 g, n=15). Each cohort of animals was divided into five groups

(n=3/treatment): (1) a sham group; (2) IV M-PFC NP (2.5 mL/kg, 0.9 g PFC/kg) sacrificed at 24 h; (3) bilateral IT M-PFC NP (2.5 mL/kg, 0.9 g PFC/kg) sacrificed at 24 h; (4) IV M-PFC NP (2.5 mL/kg, 0.9 g PFC/kg) sacrificed at 7 d; or (5) bilateral IT M-PFC NP (2.5 mL/kg, 0.9 g PFC/kg) sacrificed at 7 d. Blood samples were submitted for electrolytes, hematology, liver function and renal function.

Rabbit Vx2 lung xenograft model

The Vx2 tumors, a squamous carcinoma derived originally from Rous sarcoma virus tumor in rabbits [27], were surgically implanted into New Zealand white rabbits (2.0–2.5 kg) in the right lung proximate to the hilum. Rabbits were fasted 12 h prior to anesthesia. Atropine (0.05 mg/kg) was injected intramuscularly 15 min prior to anesthesia followed by 3% pentobarbital (30 mg/kg) via an indwelling ear vein catheter. Two or three Vx2 tumor fragments (1 mm³ each) were implanted in the hind limb of a donor rabbit, and a tumor grew to a desirable size (~20 mm diameter) in 2 weeks. The tumor was surgically removed from the donor rabbit under general anesthesia (as above) and minced into 1 mm³ fragments. The anesthetized recipient rabbit was positioned supine. The surgical area on the chest was shaved, prepped and draped. Under CT guidance, an 18 ga needle was percutaneously inserted into the right lung and positioned in the right lobe proximal to the hilum. Two fragments of minced Vx2 tumor were implanted through a 20 ga aspiration needle. Following extraction of the needle, the incision point was disinfected and sterile dressings were applied. Rabbits recovered from anesthesia and were allowed food and water *ad libitum*. Two weeks after tumor implantation, CT (GE Discovery VCT64) was used to confirm tumor development and size.

MRI Study

Longitudinal relaxation time measurements and T1 mapping were performed using a GE W750 clinical 3.0T scanner. ¹⁹F MR imaging was performed on a Philips Achieva 3.0T scanner. Relaxivity r₁ was determined by linear fits of R₁ versus [Gd]. Particulate concentration was calculated based on the total volume of NPs divided by single particle volume $(4/3)\pi r^3$, where r was nominal particle size based on DLS testing. A T1w fast spin echo sequence (FSE) at ambient room temperature was used for scanning.

Animals for T1 imaging were anesthetized with 2% isoflurane. Vx2 rabbits were administered M-PFC NPs by IV or IT (n=3, 1 mL/kg, pre-saturated with O₂), using a double-blind protocol. Coronal ¹H MR images were acquired pre-contrast and subsequently

at 1, 2, 3, 7, 12, 24, 48, 72 h using a facet joint coil. The MR imaging parameters were: T1w FSE sequence Echo Train Length:2, TE:9.3 ms, TR:1200 ms, slice thickness: 5 mm, field of view (FOV): 12×12, matrix size:288×256, flip angle:90°. For T1 mapping a T1 FSE sequence with the same parameters as above was employed except the flip angle was 111° and TEs were 50, 100, 300, 500, 700, 900, 1200, 1500, 1800, 2100, 2500 ms.

For ¹⁹F imaging, the rabbits were anesthetized with Zoletil 50 solution by intramuscular injection (Virbac (Australia) Pty Limited, Milperra, Australia). An initial ¹H acquisition for anatomical detail was performed using a fast gradient echo technique with the body coil (transmit/receive). Matrix: 244×195, FOV: 140 mm, reconstruction voxel size: 0.625 mm, TR/TE: 315ms/4.6ms, total scan duration: 02:04, reconstruction: 320×320, flip angle: 80°, NSA: 2. Fluorine imaging was performed with a MC-Rapid-BM-MN coil (RAPID Biomedical GmbH, Rimpfing, Germany) using a 3D fast gradient echo technique with ultrashort TE (UTE) sequence: FOV: 140 mm, TR/TE: 5.5ms/0.32ms, flip angle: 20°, slice number: 112, slice thickness: 1.25 mm, total scan duration: 04:47, reconstructed voxel size: 1.25 mm, matrix: 112×112, NSA: 2. The fluorine concentration of the reference phantom for ¹⁹F MR imaging was 0.65 M.

Histopathology and immunofluorescence

Male New Zealand white rabbits (~2 kg, n=3) were anesthetized with intramuscular ketamine and xylazine. One hind leg was shaved, prepped under sterile conditions, and infiltrated with Marcaine. A 2–3 mm³ rabbit Vx2 tumor fragment (squamous cell carcinoma, National Cancer Institute Tumor Repository, Frederick, MD, USA) was implanted at a depth of ~0.5 cm through a small incision into the popliteal fossa. Anatomical planes were closed and secured with a single absorbable suture. The skin was sealed with Dermabond® skin glue. Animals were recovered by reversing the effect of ketamine and xylazine with yohimbine. After ~7 weeks, animals were imaged with fluoroscopy to confirm metastasis from the popliteal fossa to the lungs. Animals were anesthetized with isoflurane to effect, then a catheter was passed under fluoroscopy into the right lung and the M-PFC NP dose was instilled (1 mL/kg). The rabbits recovered and were sacrificed 12 h later for microscopic examination of the airway and tumor response to the IT treatment.

The lung and tumor were harvested from the experimental animals, frozen in OCT and cryosectioned at 5 μm thickness. Routine staining including hematoxylin/eosin, CD68, CD31 and

proliferating cell nuclear antigen (PCNA) were performed. Nuclei were stained with DAPI. M-PFC NPs were observed with fluorescence microscopy (Olympus (Beijing) Sales & Service Co., Ltd., Beijing, China).

In vivo biodistribution experiment

Biodistribution of PFC NPs (1 mL/kg) delivered IT or IV was performed in two groups of normal adult KunMing white mice weighing 20-25 g (n=3/treatment). At 0.5, 2, 6, 24 and 48 h post treatment, mice were sacrificed and lung, liver, kidneys, spleen, heart, brain, intestine were excised and imaged *ex vivo* with a Xenogen IVIS spectrum imaging system (Perkin Elmer, Waltham, MA) using identical imaging settings (excitation 535 nm, emission DsRed, exposure time: 1s, binning factor: 2, F number: 4, FOV: 12.5) for all acquisitions.

Results

Synthesis and physical-chemical characterization of perfluorocarbon nanoparticles

M-PFC NPs were comprised of 20% (v/v) perfluoro-15-crown-5-ether (PFCE), 2% (w/v) lipid surfactant commixture, which is endogenous to the lung as surfactants, 1.7% (w/v) glycerin and water representing the balance. The lipid surfactant included 80 mol% DPPC, 10 mol% cholesterol, 5 mol% Gd-DTPA-phosphatidylethanolamine (Gd-DTPA-DPPE), 0.1 mol% rhodamine phospholipid, and 4.9 mol% dipalmitoylphosphatidylglycerol (DPPG). The average nominal hydrodynamic diameter of the M-PFC nanoparticles determined by DLS was 132 ± 6 nm with polydispersity index 0.14 ± 0.01 and zeta potential of -42 ± 4 mV. The morphology and height of the sample obtained by atomic force microscopy in standard tapping mode demonstrated a soft spherical particle on a surface with height and width estimates of 137 ± 16 nm and 62 ± 13 nm, respectively. The MR magnetic properties of ionic and particulate relaxivities (r1) of M-PFC were $3.5 \text{ mM}^{-1}\text{s}^{-1}$ and $20,450 \text{ mM}^{-1}\text{s}^{-1}$, respectively. The use of Gd-DTPA-PE, provided enhanced ^1H r1 relaxivity relative to Gd-DTPA-bisoleate (Gd-DTPA-BOA) studied previously [28], but the overall ^1H r1 was lower than prior PFC NP that included 20-30 mol% gadolinium-lipid chelate (**Figure 1 and Supplemental Figure S1**).

As previously mentioned, PFCs are chemically inert molecules with weak intramolecular interactions that permit significant quantities of many gases, including oxygen and carbon dioxide, to be physically dissolved [29, 30]. The capability to dissolve and

release oxygen was preserved and demonstrated for the M-PFC NP emulsion as referenced to nanopure water using a digital multi parameter meter (Multi 3430 WTW, Germany) coupled with an O_2 sensor (CelloX 325, WTW, Germany). Oxygen content in pure water and M-PFC NP (20%, v/v%) solution were determined at baseline with slowly bubbled 100% oxygen preoxygenation (5 min) followed by serial O_2 assessments every 5 min for 30 min to measure O_2 release (**Supplemental Figure S2**). The oxygen content of the M-PFC NP was higher than nanopure water; however, O_2 rate of loss from the emulsion was rapid and paralleled that of water.

The good biocompatibility and minimal cytotoxicity of perfluorocarbon emulsions with phospholipid surfactants were again appreciated following direct exposure of human bronchial epithelial (BEAS-2B) and human lung squamous carcinoma (H520) cells to M-PFC NP at low (9 mM) and high (90 mM) concentrations. TUNEL staining revealed no evidence of apoptosis in either cell type at either concentration. Further, incubation of M-PFC NP (9 mM) had negligible impact on the cell cycle progression (stages G0/G1, G2, S) of epithelial cells over 24 h (**Supplemental Figure S3 and S4**).

Clinical pathologic circulating biomarkers including electrolytes, liver function, renal function, and hematology of healthy mice given IV of M-PFC NP did not differ obviously from control counterparts receiving buffered saline. Intratracheal delivery of M-PFC NP elicited no changes in clinical pathology markers after 24 h or 168 h (7 d) of exposure (**Supplemental Tables S1 and S2**).

^1H and ^{19}F MRI of M-PFC NP following IT or IV administration

Rabbits bearing 14-day Vx2 tumors received M-PFC NP (1 mL/kg) via catheter directly into the right lung IT or by IV through ear vein injection. IT delivered M-PFC NP remained in the right lung for 72 h with no observed effects on animal behavior or respiratory function. ^1H MR of the rabbit tumors and nearby muscle tissue following IV and IT M-PFC NP administration elucidated the localization of the particles in and around the tumors (**Figure 2**). Small increases in tumor R1 following IV M-PFC NP were detected for 2 h post injection, relating to blood pool contrast effects, but these changes were not measured beyond 3 h. IV administration of the M-PFC NP maximally increased normalized R1 time in nearby muscle tissue at 30 min post treatment, then the signal steadily declined toward baseline during the next 12 h. In contradistinction, IT administration of M-PFC NP markedly increased tumor R1 response progressively over 12 h and this strong enhancement

persisted for 72 h. These data suggested that the M-PFC NP given IT accumulated slowly and remained confined locally in the lung Vx2 tumors; whereas, the same particles given IV failed to effectively extravasate into the cancer. Moreover, the strong increase in tumor ¹H R1 with M-PFC NP given

IT suggest that the payload of particles accumulated in the lesion was large, particularly since the ¹H relaxivity of the M-PFC NP studied was low. These superior MR data clearly suggest a theranostic potential for IT PFC NP administration in lung cancer.

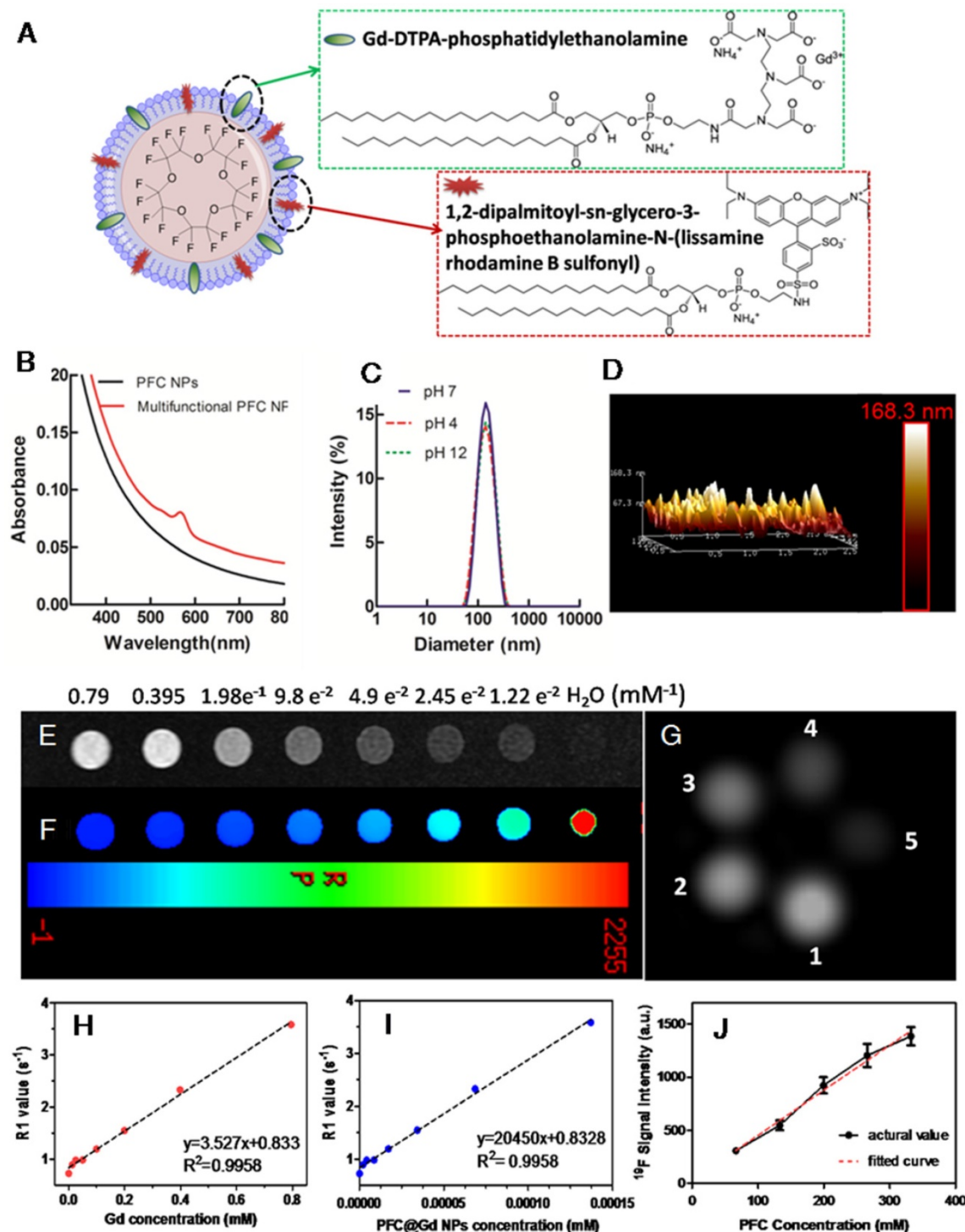


Figure 1. Physicochemical characterization of multifunctional perfluorocarbon nanoparticles. (A) Schematic representation of the structure of M-PFC NPs. (B) UV-Vis absorption spectra of PFC NPs with and without inclusion of rhodamine-PE. (C) DLS nominal hydrodynamic diameter of the multifunctional PFCs in aqueous solution was ~132 nm with stability across a wide pH range (4-12). (D) Particle morphology and height obtained from AFM. (E) T1w MR images. (F) T1 map images as a function of Gd ion concentration; (G) ¹⁹F phantom images for decreasing PFC concentration (From 1 to 5: 332, 265, 199, 132, 66 mM); ¹H R1 as a function of (H) Gd ion and (I) particulate concentration. Slopes provide r1; (J) Linear fit between ¹⁹F signal intensity and PFC concentration.

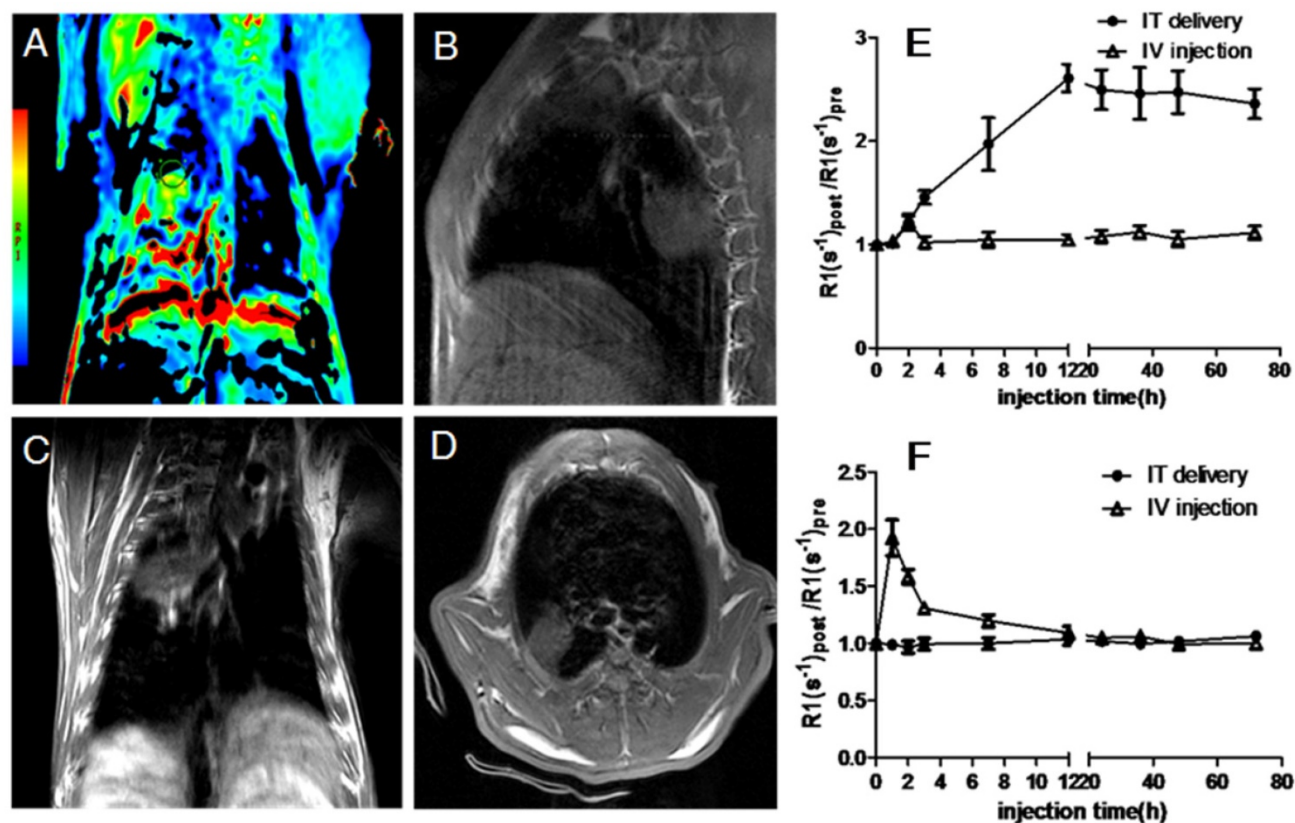


Figure 2. Representative images of *in vivo* T1w MRI after IT delivery of M-PFC NPs. (A) T1 color mapped MR images normalized to baseline; T1w MR images of (B) sagittal view, (C) coronal view, (D) transverse view; (E) and (F), the quantitative calculation of the enhancement at tumor (E) and muscle (F) sites and their specific value of R1 after different administration points (the error bars represent the standard deviations of three independent measurements of the same group).

Pulmonary ^{19}F imaging of the tumor with the M-PFC NP using the same IT delivery protocol mirrored the marked ^1H R1 mapping results closely. ^{19}F signal was visually prominent in the Vx2 tumor at 1 h and this strong signal persisted over 72 h, as shown in **Figure 3**. ^{19}F imaging with paramagnetic PFC nanoparticles is inherently less sensitive than ^1H imaging due to the relative paucity of fluorine atoms per voxel and lower NMR sensitivity of 0.83. However, the magnitude of the ^{19}F signal can be enhanced when gadolinium-lipid chelates, such as Gd-DTPA-BOA, that position the metal very close to the PFC core are included in the lipid surfactant [22, 31-33]. In the present study the low level of Gd-DTPA-PE placed the metal further away from the PFC molecules into the surrounding water, providing minimal benefit to the ^{19}F signal.

M-PFC NP utilized perfluorocrown ether (PFCE) (15:5) to maximize ^{19}F signal by increasing the number of iso-resonant fluorine atoms and to offset the possibility that the particles localizing in the tumor would be too few to detect. Yet, the tumor ^1H R1 increase achieved with M-PFC NP was very high, as was the ^{19}F signal. These data showed that intact M-PFC NP entered the tumor with the surfactant and PFC core maintained together.

Microscopy of implanted and metastatic Vx2 lung cancer

Consistent with previous studies in which paramagnetic PFC nanoparticles, both targeted and non-targeted, were administered intravenously to rabbits bearing Vx2 tumors in the popliteal fossa [24-26], rabbits with pulmonary tumors given fluorescent M-PFC NP IV showed negligible permeation of the particles into the cancer (**Figure 4**). This result corroborated the lack of persistent MR signal appreciated in the lung following M-PFC NP IV treatment. In contradistinction, microscopy of the pulmonary Vx2 cancer 72 h after IT M-PFC NP revealed deep penetration into the tumor with very dense particle coating around the tumor and stromal cells. By comparison, adjacent tumor-free lung tissue was non-consolidated and showed no evidence of fluorescent M-PFC NPs in the parenchyma (**Figure 4A**). The surfactant fluorescent dye, which could be considered as a surrogate therapeutic biomarker, labeled most of the cells in the lesion.

A second cohort of rabbits ($n=3$) with Vx2 tumor implanted in the popliteal fossa metastasized spontaneously to the lung in 7 weeks. Fluorescent M-PFC NP were delivered IT into the right bronchus

and remained for 12 h. Following sacrifice, the pulmonary airways were excised, sectioned and reviewed microscopically. Segments of the airway without Vx2 tumor metastases were devoid of nanoparticles and without inflammation. In other regions, metastatic tumors were observed adjacent to the airways and fluorescent M-PFC NP were distributed densely throughout the tumor (**Figure 4B**). The surrounding airway epithelium had minimal fluorescent dye uptake. Possibly the mucous barrier and ciliary clearance mechanism that protectively transports foreign particles from the lungs constituted a barrier between the particle lipid surface and epithelial cell membrane.

In both models, IT M-PFC NP penetrated deep into the Vx2 tumors and transferred the fluorescent lipid dye to cancer and other cells seen. Although the M-PFC NP administered IT were not targeted, their dense accumulation and prolonged contact with cells in the tumor led to a similar end result. Interestingly, the central necrotic cores of these metastatic tumors were devoid of fluorescent M-PFC NP, suggesting a difference in lung tumor development between implanted cancer pieces and spontaneously metastatic cells.

Biodistribution of nanoparticles given intratracheal versus intravenous

Tissue biodistribution study of fluorescent M-PFC NP (**Figure 5**) was studied in mice using a Xenogen IVIS imaging system, recognizing that rodents, unlike humans or rabbits, uniquely excrete nanoparticles rapidly into the small intestine via the biliary system [34]. As has been long appreciated for PFC NP [35, 36], M-PFC NPs given IV distributed to the spleen, liver and intestine at 30 min with little or no appreciable signal in the heart, lung or brain, which is also consistent with previous studies [37]. Between 6 and 24 h, IV M-PFC NP concentrations in the liver and spleen declined, with the fluorescence signal shifting to the bowel. By comparison, IT M-PFC NP distributed into the airway and lung with no systemic accumulation observed in the liver, spleen, or intestine over the course of the study. These data are consistent with MR imaging data in rabbits and suggest that IV administered M-PFC NP do not easily extravasate into tumors [24-26]; conversely IT administered particles were constrained within the tumor. Ultimately, bioelimination of PFC NP, whether administered IV or IT, eventually occurs through pulmonary exhalation of volatilized PFC [38], with the surfactant lipid components metabolized or excreted from the body. The benign PFC expiratory clearance mechanism combined with the potential to dissolve and locally release inspired oxygen from

within the tumor suggests an advantage for IT PFC NP.

Discussion

Lung cancer often presents in its late stages with cough and hemoptysis associated with tumor erosion into the airway. The prognosis for these patients is grim and palliative therapy often has limited benefit. Yet, in these poor prognosis situations, tumor disruption through the airway epithelial barrier may offer uncommon drug access into the lesion via intratracheal delivery. Typically, pulmonary inhalation of drugs and particles, whether therapeutic or via environmental exposure, can elicit pulmonary inflammation and respiratory dysfunction. Although intended for local delivery, IT delivery of nanoparticles frequently permeates further into the circulation, decreasing the level of therapy retained in the lung and increasing the risk of systemic off-target effects [39]. As an example, the orotracheal delivery of ultrasmall gadolinium oxide nanoparticles was shown to effectively penetrate into lung tumor but then continued to diffuse into the circulation and subsequently collected in the kidney [40]. Some inhaled particles, such as large iron oxide nanoparticles (100 nm), elicit strong inflammatory responses and elevated chemokine secretions [41]. Titanium oxide (TiO₂) nanoparticles, known to cause renal fibrosis when injected systemically, were found to elicit dose-dependent pathological changes in the kidney via IT delivery as well as emphysema-like lung injury [42, 43]. Clearly, the intended localized high dose and safety benefits attributed to IT nanoparticle delivery can be compromised when the minute size of these agents permits penetration into the systemic circulation or when the chemical composition is inflammatory.

Perfluorocarbons inherently have high biocompatibility and a capacity to dissolve oxygen that was dramatically demonstrated by liquid-ventilation, i.e., liquid breathing, in rodents in 1966 [44]. Continued research with PFC nanoparticles led to a seminal clinical demonstration of improved pulmonary function in neonatal infants suffering with respiratory distress syndrome in 1996 [15]. These fragile neonates receiving intratracheal PFC NP experienced improved respiratory function with negligible adverse effects. Over the last 25 years, PFC NPs have been extensively explored in both preclinical and clinical realms. Applications involving IV administration of PFC NP include blood pool imaging, inflammation imaging, cell tracking, thrombus detection and treatment, angiogenesis imaging and drug delivery in cancer, atherosclerosis, and rheumatoid arthritis models, etc. [45-48].

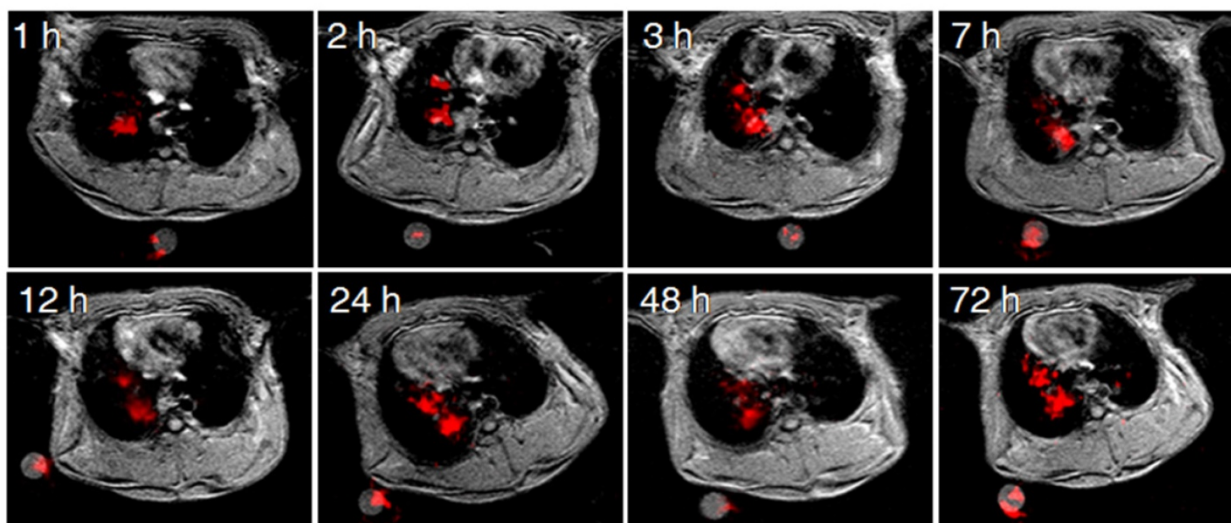


Figure 3. Dynamic monitoring of ¹⁹F-MR enhancement at different time points post IT delivery of the M-PFC NPs. Image slices were acquired at different time points and examples selected to depict similar cardiothoracic regions.

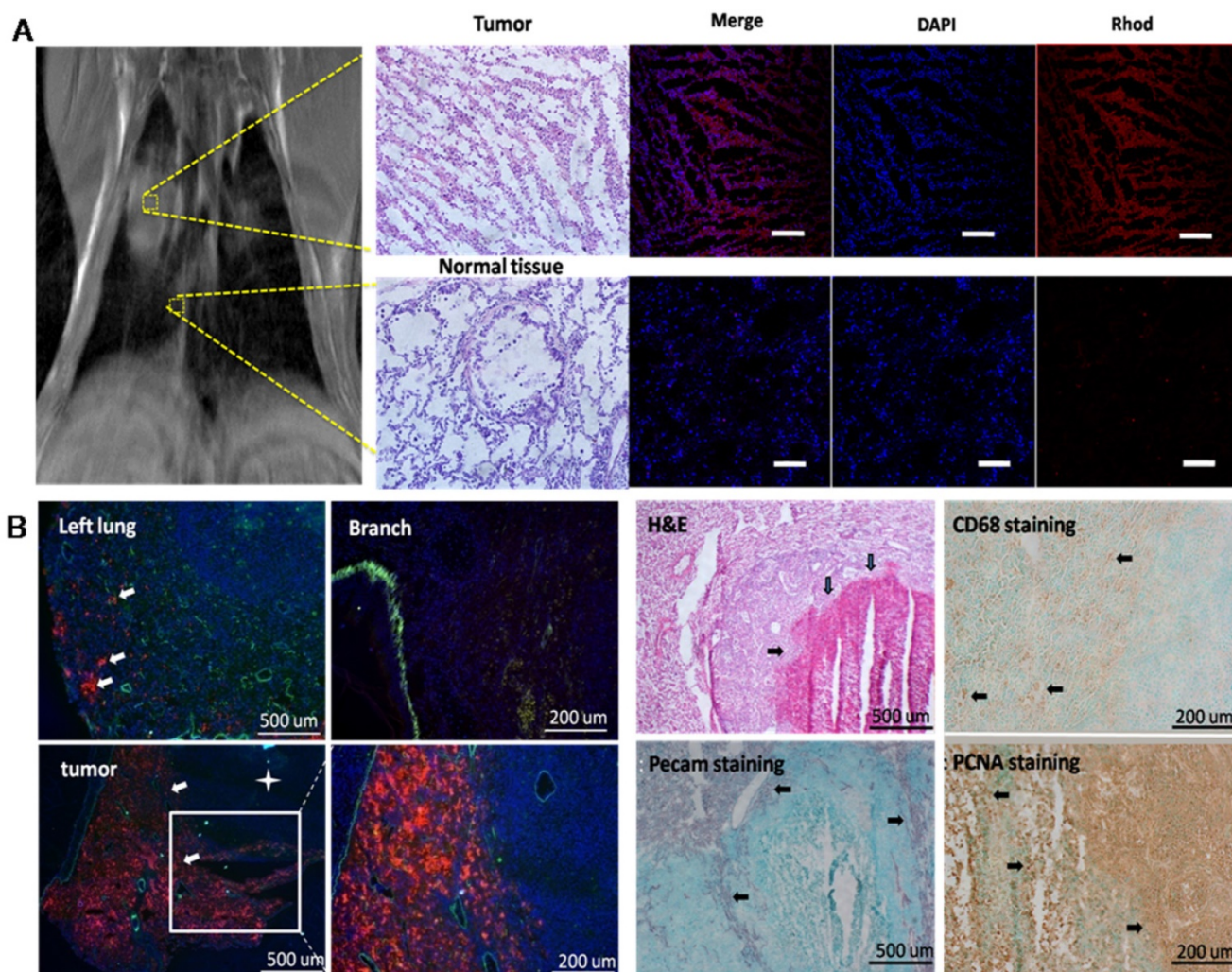


Figure 4. (A) Microscopy of rabbits receiving *in situ* surgical implantation, following IT treatment. The upper row represents the typical images harvested from lung tumor 72 h after MR study. Fluorescence microscopy images of tumor tissue with DAPI stained nuclei (blue) and Rhod B (red) fluorescence from M-PFC NP. Normal tissue from the same rabbit with no M-PFC NP signal (scale bars = 100 μm). (B) Microscopic imaging of metastatic carcinoma Vx2 tumor model. While the left lung showed low tumor burden, the right lung had tumors with high density M-PFC NP signal (red) around the tumor periphery. H&E staining of lung tumor (white box, expanded) revealed a necrotic core (arrows), which is also indicated by a star in the lower magnification image. CD68 macrophages were noted around the tumor capsule. PECAM stained blood vessels were also mostly peripheral around the tumor capsule (arrows). Proliferating PCNA positive cells were best observed within the metastatic tumor and around its capsule.

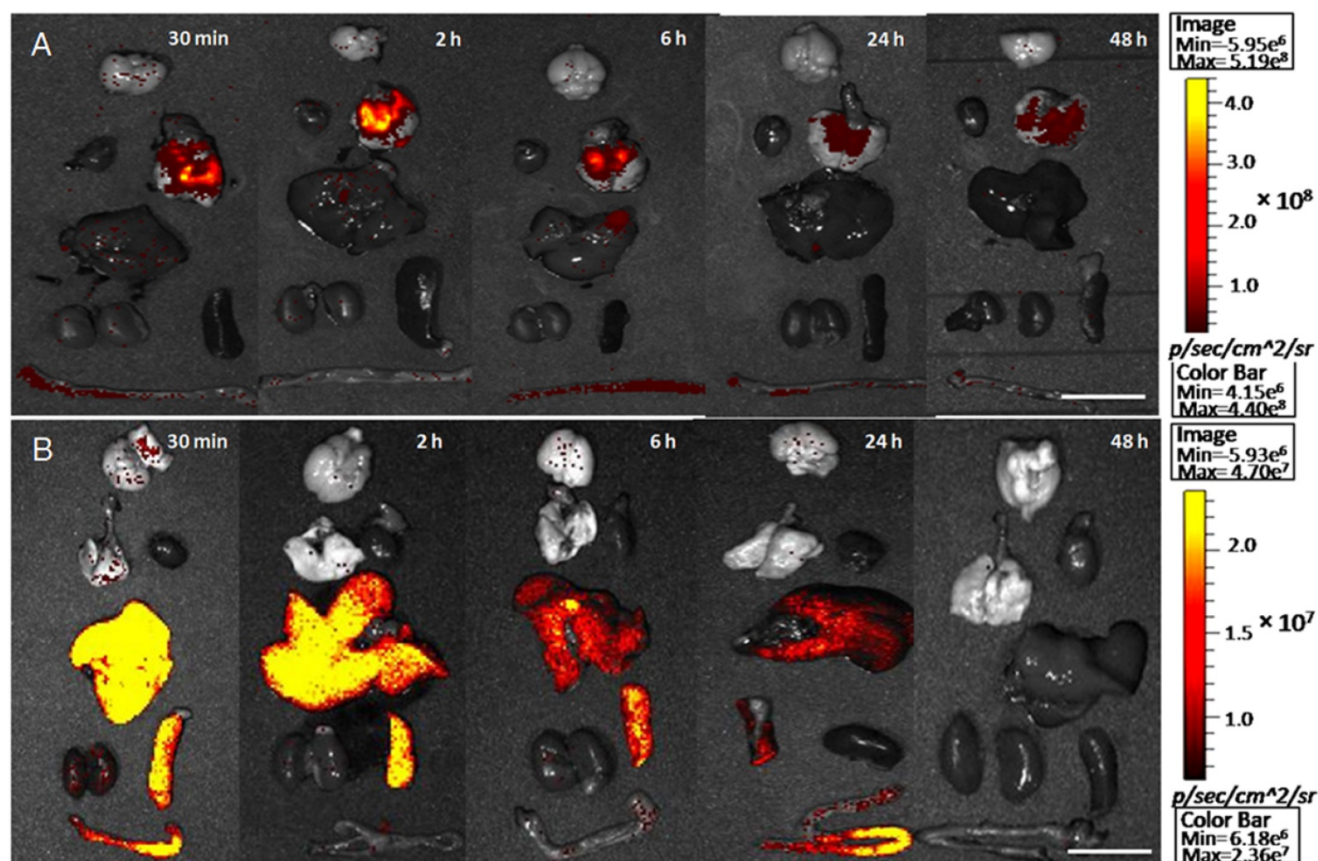


Figure 5. The biodistribution of M-PFC nanoparticles with time-dependent isolated organs as seen using the NIRF imaging technique. (A) Intratracheal delivery; (B) intravenous injection. (scale bars=1 cm)

In the present study, the high biocompatibility, ideal size, oxygen dissolving capacity and natural bioelimination via exhalation contributed to the success of M-PFC NP in the Vx2 rabbit lung tumor model. As evidenced by ^1H and ^{19}F MR imaging, the IT M-PFC NP penetrated into the growing Vx2 tumor, slowly and progressively over 12 h and persisted for 72 h. The magnitude and persistence of M-PFC NP via intratracheal delivery into the tumor was dramatically better than the minimal and transient MR T1 signal response noted at 2 h following IV injection. Moreover, IT M-PFC NP were essentially confined to the cancer, lung and airways, whereas, the biodistribution of IV M-PFC NP extended beyond with systemic accumulation in the liver and spleen.

Extravascular distribution of nanoparticles into tumors following intravenous injection remains a significant barrier to the clinical translation of nanotechnology [49]. Although some particles are capable of penetrating beyond the circulation and into the tumor, inhomogeneous distribution within the lesion with large portions of the cancer unaffected is common [50]. Intratumoral delivery by IT M-PFC NP had very homogeneous distribution, excluding only the necrotic regions. In each animal, the IT fluorescent

M-PFC NP densely coated the tumor cells and their microenvironment, which was evidenced by the strong T1 shortening and prominent ^{19}F signals measured with MRI.

The prolonged tumoral persistence of the ^{19}F and ^1H signal administered IT also reflects the very long biological half-life of PFCE (250d, 9.4T) as compared with perfluorooctylbromide (PFOB, 12d, 9.4T) used previously in clinical studies [51]. In humans, the biological half-life estimate for PFOB is typically cited as 3-4 d, while PFCE intrapulmonary persistence is clinically too long (>60 d) [52]. Recently, ^{19}F neovascular molecular imaging studies at 3T (clinical) utilized $\alpha_v\beta_3$ -targeted PFOB nanoparticles to detect the sparse $\alpha_v\beta_3$ -intergrin expression of pulmonary neovasculation in rat models of acute lung ischemia and asthma [53-55]. These data considered in combination with the strong serial $^1\text{H}/^{19}\text{F}$ data presented in this report suggest that substitution of PFCE with PFOB would not compromise the theranostic potential of the nanoplatform approach.

Although the treatment of lung cancer was beyond the scope of this proof-of-concept imaging study, the potential for effective lung cancer treatment with IT delivered PFC NP was suggested by the broad

transfer of rhodamine-lipid dye to intratumoral cells observed with microscopy. The formation of these irreversible lipid fusion complexes facilitates the delivery of drug payloads into cells via "contact facilitated drug delivery" [56]. Moreover, the dense delivery of continuously oxygenated PFC NP within an otherwise hypoxic tumor may offer potent radio-sensitization for focal radiation or PDT therapy guided by ^{19}F -MRI [57-60]. The use of therapeutic drugs in combination with IT administered PFC NP may be a highly effective delivery approach for lung cancer warranting further research.

Conclusion

Lipid-encapsulated M-PFC NP were administered via intratracheal delivery into rabbits bearing pulmonary Vx2 tumors implanted surgically or formed by metastasis. Enhanced intratumoral penetration of intact paramagnetic PFC nanoparticles by IT administration was demonstrated for the first time by ^{19}F and ^1H MR using clinical 3T scanners. The PFC particles persisted for over 72 h *in vivo* without adverse effects on rabbit behavior or respiration. Fluorescence microscopy corroborated that IT M-PFC NP permeated deeply and distributed widely throughout the tumors. In contradistinction, IV M-PFC NP did not extravasate into the lung cancers and provided much lower transient tumor contrast enhancement, consistent with a blood pool effect. By the IT route, M-PFC NP uptake was confined to the Vx2 cancer without significant permeation into the general circulation. By comparison, IV administration of M-PFC NP resulted in transient enhancement of highly vascular muscle tissues with typical RES clearance by the liver and spleen. This proof-of-concept study returns the focus of PFC NP delivery from intravenous applications to intratracheal use to address the unmet challenges posed by lung cancer.

Abbreviations

^{19}F : fluorine-19; IT: intratracheal delivery; IV: intravenous injection; PFC: perfluorocarbon; NSCLC: non-small cell lung cancer; MRI: magnetic resonance imaging; UTE: ultrashort echo time sequences; FSE: fast spin echo sequence; NA: number of average; DLS: dynamic light scattering; FSE: fast spin echo sequence; TE: echo time; TR: repetition time; FOV: field of view; TUNEL: TdT-mediated dUTP nick end labeling; H&E: hematoxylin and eosin; PDT: photodynamic therapy.

Supplementary Material

Supplementary figures and tables.

<http://www.thno.org/v08p0563s1.pdf>

Acknowledgments

This work was supported by the National Basic Research Program of China (2015CB931800), National Natural Science Foundation of China (81627901, 31210103913) and the Key Laboratory of Molecular Imaging Foundation (College of Heilongjiang Province). LNW expressed appreciation to the support of National Natural Science Foundation of China (81771903), Natural Science Foundation of Heilongjiang Province of China (LC2016034, LC2013C26), the Youth Science WU LIANDE Foundation of Harbin Medical University (WLD-QN1404, WLD-QN1119), Heilongjiang Postdoctoral Funds for Scientific Research Initiation (No. LBH-Q15090), the Fourth Hospital of Harbin Medical University Fund for Distinguished Young Scholars (HYDSYJQ201601). This research was further supported in whole or part by grants from the CA154737 (GML), CA199092 (GML) HL122471 (GML), HL112518 (GML), HL113392 (GML) and an HHSN26820140042C (GML), Additional support for the MR scanners was provided by the Foundation for Barnes Jewish Hospital.

Competing Interests

The authors have declared that no competing interest exists.

References

1. Ervik M, Lam F, Ferlay J, Mery L, Soerjomataram I, Bray F. International Agency for Research on Cancer, Cancer fact sheets: lung cancer. *Cancer Today*. Lyon, France; 2016.
2. Siegel R, Miller K, Jemal A. *Cancer Statistics, 2016*. *CA Cancer J Clin*. 2016; 66: 7-30.
3. Gridelli C, Rossi A, Carbone D, Guarize J, Karachaliou N, Mok T, et al. Non-small Cell Lung Cancer. *Nat Rev Dis Primers*. 2015; 1: 15009.
4. Houston K, Henley S, Li J, White M, Richards T. Patterns in lung cancer incidence rates and trends by histologic type in the United States, 2004-2009. *Lung Cancer*. 2014; 86: 22-8.
5. Chien C, Liang J, Chen J, Wang H, Lin C, Chen C, et al. ^{18}F Fluorodeoxyglucose-positron emission tomography screening for lung cancer: a systematic review and meta-analysis. *Cancer Imaging*. 2013; 13: 458-65.
6. Islam S, Walker R. Advanced imaging (positron emission tomography and magnetic resonance imaging) and image-guided biopsy in initial staging and monitoring of therapy of lung cancer. *Cancer J*. 2013; 19: 208-16.
7. Oki M, Saka H, Kitagawa C, Tanaka S, Shimokata T, Mori K, et al. Novel thin bronchoscope with a 1.7-mm working channel for peripheral pulmonary lesions. *Eur Respir J*. 2008; 32: 465-71.
8. Bose S, Ghatol A, Eberlein M, Yung R. Ultrathin bronchoscopy in the diagnosis of peripheral cavity lung lesions. *J Bronchology Interv Pulmonol*. 2013; 20: 167-70.
9. Keupp J, Rahmer J, Grässlin I, Mazurkewitz PC, Schaeffter T, Lanza GM, et al. Simultaneous dual-nuclei imaging for motion corrected detection and quantification of ^{19}F imaging agents. *Magn Reson Med*. 2011; 66: 1116-22.
10. Goette MJ, Keupp J, Rahmer J, Lanza GM, Wickline SA, Caruthers SD. Balanced UTE-SSFP for ^{19}F MR imaging of complex spectra. *Magnetic Resonance in Medicine*. 2015; 74: 537-43.
11. Schmieder AH, Caruthers SD, Keupp J, Wickline SA, Lanza GM. Recent Advances in ^{19}F Fluorine Magnetic Resonance Imaging with Perfluorocarbon Emulsions. *Engineering*. 2016; 1: 475-89.
12. Bulte JW. Hot spot MRI emerges from the background. *Nat Biotechnol*. 2005; 23: 945-6.
13. Greenspan JS, Wolfson MR, Rubenstein SD, Shaffer TH. Liquid ventilation of human preterm neonates. *J Pediatr*. 1990; 117: 106-11.
14. Leach CL, Holm B, Morin FC, 3rd, Fuhrman BP, Papo MC, Steinhorn D, et al. Partial liquid ventilation in premature lambs with respiratory distress syndrome: efficacy and compatibility with exogenous surfactant. *J Pediatr*. 1995; 126: 412-20.

15. Leach CL, Greenspan JS, Rubenstein SD, Shaffer TH, Wolfson MR, Jackson JC, et al. Partial liquid ventilation with perflubron in premature infants with severe respiratory distress syndrome. The LiquiVent Study Group. *N Engl J Med.* 1996; 335: 761-7.
16. Kendig JW, Notter RH, Cox C, Aschner JL, Benn S, Bernstein RM, et al. Surfactant replacement therapy at birth: final analysis of a clinical trial and comparisons with similar trials. *Pediatrics.* 1988; 82: 756-62.
17. Liechty EA, Donovan E, Purohit D, Gilhooly J, Feldman B, Noguchi A, et al. Reduction of neonatal mortality after multiple doses of bovine surfactant in low birth weight neonates with respiratory distress syndrome. *Pediatrics.* 1991; 88: 19-28.
18. Schneider P. Artificial blood substitutes. *Transfus Sci.* 1992; 13: 357-70.
19. Flacke S, Fischer S, Scott M, Fuhrhop R, Allen J, Mc Lean M, et al. A novel MRI contrast agent for molecular imaging of fibrin: implications for detecting vulnerable plaques. *Circulation.* 2001; 104: 1280-5.
20. Ahrens ET, Bulte JWM. Tracking immune cells in vivo using magnetic resonance imaging. *Nat Rev Immunol.* 2013; 13: 755-63.
21. Li C. A targeted approach to cancer imaging and therapy. *Nat Mater.* 2014; 13: 110-5.
22. Kislukhin AA, Xu H, Adams SR, Narsinh KH, Tsien RY, Ahrens ET. Paramagnetic fluorinated nanoemulsions for sensitive cellular fluorine-19 magnetic resonance imaging. *Nat Mater.* 2016; 15: 662-8.
23. Zhang N, Cai X, Gao W, Wang R, Xu C, Yao Y, et al. A Multifunctional Theranostic Nanoagent for Dual-Mode Image-Guided HIFU/Chemotherapy Cancer Therapy. *Theranostics.* 2016; 6: 404-17.
24. Schmieder AH, Winter PM, Williams TA, Allen JS, Hu G, Zhang H, et al. Molecular MR imaging of neovascular progression in the Vx2 tumor with alpha(v)beta3-targeted paramagnetic nanoparticles. *Radiology.* 2013; 268: 470-80.
25. Winter PM, Caruthers SD, Kassner A, Harris TD, Chinen LK, Allen JS, et al. Molecular imaging of angiogenesis in nascent Vx-2 rabbit tumors using a novel alpha(nu)beta3-targeted nanoparticle and 1.5 tesla magnetic resonance imaging. *Cancer Res.* 2003; 63: 5838-43.
26. Winter PM, Schmieder AH, Caruthers SD, Keene JL, Zhang H, Wickline SA, et al. Minute dosages of alpha(nu)beta3-targeted fumagillin nanoparticles impair Vx-2 tumor angiogenesis and development in rabbits. *FASEB J.* 2008; 22: 2758-67.
27. Rous P, Kidd J, Smith W. Experiments on the cause of rabbit carcinoma derived from virus-induced papillomas. Loss by Vx2 carcinoma to immunize hosts against papilloma virus. *J Exp Med.* 1952; 96: 159-74.
28. Winter P, Caruthers S, Yu X, Song S, Fuhrhop R, Chen J, et al. Improved molecular imaging contrast agent for detection of human thrombus. *Magn Reson Med.* 2003; 50: 411-6.
29. O'Brien RN, Langlais AJ, Seufert WD. Diffusion coefficients of respiratory gases in a perfluorocarbon liquid. *Science.* 1982; 217: 153-5.
30. Fuhrman BP, Paczan PR, DeFrancis M. Perfluorocarbon-associated gas exchange. *Crit Care Med.* 1991; 19: 712-22.
31. Caruthers SD, Neubauer AM, Hockett FD, Lamerichs R, Winter PM, Scott MJ, et al. In vitro demonstration using (19)F magnetic resonance to augment molecular imaging with paramagnetic perfluorocarbon nanoparticles at 1.5 Tesla. *Invest Radiol.* 2006; 41: 305-12.
32. Neubauer AM, Myerson J, Caruthers SD, Hockett FD, Winter PM, Chen J, et al. Gadolinium-modulated 19F signals from perfluorocarbon nanoparticles as a new strategy for molecular imaging. *Magn Reson Med.* 2008; 60: 1066-72.
33. de Vries A, Moonen R, Yildirim M, Langereis S, Lamerichs R, Pikkemaat JA, et al. Relaxometric studies of gadolinium-functionalized perfluorocarbon nanoparticles for MR imaging. *Contrast Media Mol Imaging.* 2014; 9: 83-91.
34. Bulte JWM, Schmieder AH, Keupp J, Caruthers SD, Wickline SA, Lanza GM. MR cholangiography demonstrates unsuspected rapid biliary clearance of nanoparticles in rodents: Implications for clinical translation. *Nanomedicine.* 2014; 10: 1385-8.
35. Mattrey RF, Long DM, Multer FK, Mitten R, Higgins CB. Perfluoroctylbromide: a reticuloendothelial-specific and tumor-imaging agent for computed tomography. *Radiology.* 1982; 145: 755-8.
36. Bruneton JN, Falewee MN, Balumaestro C, Normand F, Mattrey RF. Perfluoroctylbromide and hepatosplenic computed tomography. Preliminary clinical study. *Investigative Radiology.* 1988; 23.
37. Wu L, Cai X, Nelson K, Xing W, Xia J, Zhang R, et al. A green synthesis of carbon nanoparticles from honey and their use in real-time photoacoustic imaging. *Nano Research.* 2013; 6: 312-25.
38. Cohn CS, Cushing MM. Oxygen therapeutics: perfluorocarbons and blood substitute safety. *Crit Care Clin.* 2009; 25: 399-414.
39. Choi HS, Ashitate Y, Lee JH, Kim SH, Matsui A, Insin N, et al. Rapid translocation of nanoparticles from the lung airspaces to the body. *Nature biotechnology.* 2010; 28: 1300-3.
40. Bianchi A, Dufort S, Lux F, Fortin PY, Tassali N, Tillement O, et al. Targeting and in vivo imaging of non-small-cell lung cancer using nebulized multimodal contrast agents. *Proceedings of the National Academy of Sciences of the United States of America.* 2014; 111: 9247-52.
41. Park EJ, Oh SY, Lee SJ, Lee K, Kim Y, Lee BS, et al. Chronic pulmonary accumulation of iron oxide nanoparticles induced Th1-type immune response stimulating the function of antigen-presenting cells. *Environmental research.* 2015; 143: 138-47.
42. Chen HW, Su SF, Chien CT, Lin WH, Yu SL, Chou CC, et al. Titanium dioxide nanoparticles induce emphysema-like lung injury in mice. *FASEB journal :* official publication of the Federation of American Societies for Experimental Biology. 2006; 20: 2393-5.
43. Tang Y, Wang F, Jin C, Liang H, Zhong X, Yang Y. Mitochondrial injury induced by nanosized titanium dioxide in A549 cells and rats. *Environmental toxicology and pharmacology.* 2013; 36: 66-72.
44. Clark LC, Jr., Gollan F. Survival of mammals breathing organic liquids equilibrated with oxygen at atmospheric pressure. *Science.* 1966; 152: 1755-6.
45. Yue X, Wang Z, Zhu L, Wang Y, Qian C, Ma Y, et al. Novel 19F activatable probe for the detection of matrix metalloproteinase-2 activity by MRI/MRS. *Molecular Pharmaceutics.* 2014; 11: 4208-17.
46. Barshir A, Yadav NN, Gilad AA, Van Zijl PCM, McMahon MT, Bulte JWM. Single (19)F probe for simultaneous detection of multiple metal ions using miCEST MRI. *Journal of the American Chemical Society.* 2015; 137: 78.
47. Ye YX, Basse-Lusebrink TC, Arias-Loza PA, Kocoski V, Kampf T, Gan Q, et al. Monitoring of monocyte recruitment in reperfused myocardial infarction with intramyocardial hemorrhage and microvascular obstruction by combined fluorine 19 and proton cardiac magnetic resonance imaging. *Circulation.* 2013; 128: 1878-88.
48. Shin SH, Park EJ, Min C, Choi SI, Jeon S, Kim YH, et al. Tracking Perfluorocarbon Nanoemulsion Delivery by 19F MRI for Precise High Intensity Focused Ultrasound Tumor Ablation. *Theranostics.* 2017; 7: 562-72.
49. Thakor AS, Gambhir SS. Nanooncology: The future of cancer diagnosis and therapy. *CA: A Cancer Journal for Clinicians.* 2013; 63: 395-418.
50. Chen H, Zhang W, Zhu G, Xie J, Chen X. Rethinking cancer nanotheranostics. *Nat Rev Mater.* 2017; 2: 17024.
51. Jacoby C, Temme S, Mayenfels F, Benoit N, Krafft MP, Schubert R, et al. Probing different perfluorocarbons for in vivo inflammation imaging by 19F MRI: image reconstruction, biological half-lives and sensitivity. *NMR Biomed.* 2014; 27: 261-71.
52. Krafft MP. Fluorocarbons and fluorinated amphiphiles in drug delivery and biomedical research. *Advanced Drug Delivery Reviews.* 2001; 47: 209-28.
53. Schmieder AH, Wang K, Zhang H, Senpan A, Pan D, Keupp J, et al. Characterization of early neovascular response to acute lung ischemia using simultaneous 19F/1H MR molecular imaging. *Angiogenesis.* 2014; 17: 51-60.
54. Wagner EM, Jenkins J, Schmieder A, Eldridge L, Zhang Q, Moldobaeva A, et al. Angiogenesis and airway reactivity in asthmatic Brown Norway rats. *Angiogenesis.* 2015; 18: 1-11.
55. Lanza GM, Jenkins J, Schmieder AH, Moldobaeva A, Cui G, Zhang H, et al. Anti-angiogenic nanotherapy inhibits airway remodeling and hyper-responsiveness of dust mite triggered asthma in the Brown Norway rat. *Theranostics.* 2017; 7: 377-89.
56. Pan D, Pham CT, Weillbaecher KN, Tomasson MH, Wickline SA, Lanza GM. Contact-facilitated drug delivery with Sn2 lipase labile prodrugs optimize targeted lipid nanoparticle drug delivery. *Wiley interdisciplinary reviews Nanomedicine and nanobiotechnology.* 2016; 8: 85-106.
57. Cheng Y, Cheng H, Jiang C, Qiu X, Wang K, Huan W, et al. Perfluorocarbon nanoparticles enhance reactive oxygen levels and tumour growth inhibition in photodynamic therapy. *Nature Communications.* 2015; 6: 8785.
58. Huang L, Li Z, Zhao Y, Zhang Y, Wu S, Zhao J, et al. Ultralow-Power Near Infrared Lamp Light Operable Targeted Organic Nanoparticle Photodynamic Therapy. *Journal of the American Chemical Society.* 2016; 138: 14586-91.
59. Ke H, Wang J, Tong S, Jin Y, Wang S, Qu E, et al. Gold nanoshelled liquid perfluorocarbon magnetic nanocapsules: a nanotheranostic platform for bimodal ultrasound/magnetic resonance imaging guided photothermal tumor ablation. *Theranostics.* 2013; 4: 12-23.
60. Song X, Feng L, Liang C, Yang K, Liu Z. Ultrasound Triggered Tumor Oxygenation with Oxygen-Shuttle Nanoperfluorocarbon to Overcome Hypoxia-Associated Resistance in Cancer Therapies. *Nano Letters.* 2016; 16: 6145-53.